RESEARCH ARTICLE

WILEY **NMR** IN BIOMEDICINE

Quantification of liver function by linearization of a two-compartment model of gadoxetic acid uptake using dynamic contrast-enhanced magnetic resonance imaging

Josiah Simeth[1,2] (iD) | Adam Johansson[1] | Dawn Owen[1] | Kyle Cuneo[1] | Michelle Mierzwa[1] | Mary Feng[1,3] | Theodore S. Lawrence[1] | Yue Cao[1,2,4]

[1] Department of Radiation Oncology, University of Michigan, Ann Arbor, MI, USA

[2] Department of Biomedical Engineering, University of Michigan, Ann Arbor, MI, USA

[3] Department of Radiation Oncology, University of California San Francisco, San Francisco, CA, USA

[4] Department of Radiology, University of Michigan, Ann Arbor, MI, USA

Correspondence
Josiah Simeth, Department of Radiation Oncology, University of Michigan, Argus Building 1, 519 W William St, Ann Arbor, MI 48103-4943, USA.
Email: jjsimeth@umich.edu; jjsimeth@gmail.com

Funding information
Foundation for the National Institutes of Health (NIH), Grant/Award Numbers: R01 CA132834 and P01 CA059827

Dynamic gadoxetic acid-enhanced magnetic resonance imaging (MRI) allows the investigation of liver function through the observation of the perfusion and uptake of contrast agent in the parenchyma. Voxel-by-voxel quantification of the contrast uptake rate (k_1) from dynamic gadoxetic acid-enhanced MRI through the standard dual-input, two-compartment model could be susceptible to overfitting of variance in the data. The aim of this study was to develop a linearized, but more robust, model. To evaluate the estimated k_1 values using this linearized analysis, high-temporal-resolution gadoxetic acid-enhanced MRI scans were obtained in 13 examinations, and k_1 maps were created using both models. Comparison of liver k_1 values estimated from the two methods produced a median correlation coefficient of 0.91 across the 12 scans that could be used. Temporally sparse clinical MRI data with gadoxetic acid uptake were also employed to create k_1 maps of 27 examinations using the linearized model. Of 20 scans, the created k_1 maps were compared with overall liver function as measured by indocyanine green (ICG) retention, and yielded a correlation coefficient of 0.72. In the 27 k_1 maps created via the linearized model, the mean liver k_1 value was 3.93 ± 1.79 mL/100 mL/min, consistent with previous studies. The results indicate that the linearized model provides a simple and robust method for the assessment of the rate of contrast uptake that can be applied to both high-temporal-resolution dynamic contrast-enhanced MRI and typical clinical multiphase MRI data, and that correlates well with the results of both two-compartment analysis and independent whole liver function measurements.

KEYWORDS

DCE-MRI, Gd chelate based contrast agents, hepatobiliary contrast, imaging informed treatment planning, liver function, quantitative imaging

---

Abbreviations used: 3D, three-dimensional; AIF, arterial input function; DCE, dynamic contrast enhanced; DITC, dual-input, two-compartment; HCC, hepatocellular carcinoma; Hct, hematocrit; HEF, hepatic extraction fraction; HTR, high temporal resolution; ICG, indocyanine green; LLS, linear least-squares; LSITC, linearized single-input, two-compartment; LTR, low temporal resolution; MRI, magnetic resonance imaging; PET, positron emission tomography; PK, pharmacokinetic; PVIF, portal vein input function; RE, relative enhancement; SPECT, single-photon emission computed tomography; WAPE, weighted absolute percentage error; WMAPE, weighted mean absolute percentage error.

1 | INTRODUCTION

Regional and global liver function measurements are critical for guiding treatments for intrahepatic cancers, including surgical resection, radiofrequency or microwave ablation, and radiation therapy, to preserve liver function and prevent organ failure.[1] Mapping both baseline regional liver function and early change after liver-directed therapy is critical to predict permanent treatment effects on liver function and reduce the probability of liver failure after intervention. Further, accurate liver function mapping could allow for precise customization of treatment planning that carefully accounts for present and future regional liver function.[2,3]

Various methods currently exist for the determination of regional liver function. Positron emission tomography (PET) and single-photon emission computed tomography (SPECT), with radioactive hepatobiliary tracers, have been developed for the direct measurement of regional liver function.[3-5] Magnetic resonance imaging (MRI)-based methods benefit from both superior resolution and the absence of a radiation dose during the assessment scans. Using dynamic contrast-enhanced (DCE) MRI with vascular contrast agents, perfusion parameters have been calculated from a dual-input, single-compartment model of the liver, in which portal venous perfusion is considered as a surrogate for liver function.[6] However, the use of a hepatobiliary contrast agent allows direct assessment of liver function through contrast uptake in liver parenchyma. Gadoxetic acid, marketed in the USA as Eovist, and as Primovist in Europe, is a hepatobiliary MRI contrast agent.[7] It is distinguished from vascular agents in that it is taken up into liver cells, allowing more direct interrogation of liver function. Using this agent, the hepatic extraction fraction (HEF) can be estimated to assess liver function. Although HEF is directly related to the uptake rate, it cannot isolate the uptake rate from the effects of plasma flow. Semi-quantitative measures, such as relative enhancement (RE) and enhancement relative to spleen, similarly cannot differentiate between the uptake rate and plasma flow, whilst additionally either ignoring fluid enhancement or assuming its uniform conformity to fluid enhancement in the spleen.[8] A dual-input, two-compartment (DITC) model of liver function can be used to directly estimate the uptake rate, but the model requires high-temporal-resolution images to adequately characterize the concentration curves used as inputs, can have as many as six unknown parameters and may be susceptible to overfitting variance in the data.[9]

This study develops and applies a linear model based on the DITC model of liver function. Ideally, this model can be used to estimate both flow-dependent and flow-independent measures of liver function with decreased computational complexity and susceptibility to variance relative to the DITC model. To this end, we compare the results of the developed model with the DITC model as applied to high-temporal-resolution gadoxetic acid-enhanced MRI data and to indocyanine green (ICG) retention in livers with corresponding clinical temporally sparse MRI data. Through simulations, we also assess the impact of failure to capture the peak of the arterial input function (AIF) on the estimate of uptake. This allows us to confirm the correspondence of our approach to the two-compartment model for liver function, and to an independent and reliable measure of whole liver function found in the extraction by the liver of ICG,[10] whilst confirming the applicability to low-temporal-resolution clinical datasets.

2 | METHODS AND MATERIALS

2.1 | DITC model

2.1.1 | Model description

The DITC pharmacokinetic (PK) model of gadoxetic acid in the liver[9] is illustrated in Figure 1. This model describes the hemodynamics of gadoxetic acid (hepatic arterial and portal venous perfusion) and contrast uptake of hepatocytes. In this model, after injection of a bolus of gadoxetic acid, the contrast circulates in the blood by flowing in from both hepatic artery and portal vein into the sinusoids, distributing in the space of Disse and flowing out through the central and hepatic veins. This assumes fast exchange between the sinusoids and the space of Disse. Meanwhile, hepatocytes take up the contrast through the sinusoid membrane. The contrast uptake of hepatocytes is assumed to be unilateral, by omitting the minor efflux of the contrast back to sinusoids in the initial retention period.[11] This model also omits the slow and delayed excretion process.
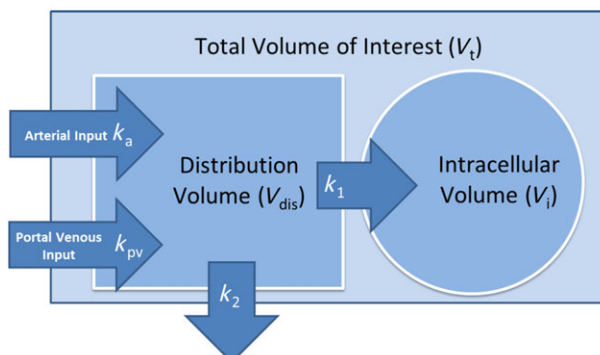

FIGURE 1 A dual-input, two-compartment pharmacokinetic model of gadoxetic acid in the liver

If we consider a voxel or a volume of interest with a total volume of V_t, the total amount of contrast in the voxel is the sum of the amounts of contrast in the extracellular and intracellular spaces, and can be described by the following equations:

$$\overbrace{V_t C_t(t)}^{\text{Contrast in Tissue}} = \overbrace{V_{dis} C_{dis}(t)}^{\text{Extracellular Contrast}} + \overbrace{k_1 \int_0^t V_{dis} C_{dis}(\tau) d\tau}^{\text{Intracellular Contrast}} \tag{1}$$

$$V_{dis} C_{dis}(t) = V_{dis} \int_0^t (k_a C_a(\tau - \tau_a) + k_{pv} C_{pv}(\tau - \tau_{pv})) e^{-(t-\tau)(k_2 + k_1)} d\tau \tag{2}$$

where V_{dis} is the distribution volume of blood; C_t, C_{dis}, C_a and C_{pv} are contrast concentrations as a function of time in the total, distribution, arterial and portal vein volumes, respectively; τ_a and τ_{pv} describe the arrival time delays of the AIF and portal vein input function (PVIF), respectively, at each voxel; k_a and k_{pv} describe the normalized arterial and portal venous flow rates, respectively; and k_2 is the normalized flow rate leaving the volume of interest through the central vein. k_1 is the normalized rate of uptake of contrast to the intracellular space. The distribution volume includes the space of Disse and sinusoids. We also define a fractional distribution volume of $v_{dis} = \dfrac{V_{dis}}{V_t}$. The derivation and a detailed description of the equations are given in Appendix A.

C_t, C_a and C_{pv} are measurable from the intensity of DCE MRI at regions or voxels of hepatic tissue, artery and portal vein, respectively. As a result, Equations 1 and 2 have six unknown variables (k_a, k_{pv}, τ_a, τ_{pv}, k_1 and v_{dis}) to be determined.

2.1.2 | Optimization

To determine the six unknown variables in Equations 1 and 2, the cost function:

$$\sum_{i=0}^{N_t - 1} \left[C_t(iT) - \hat{C}_t(iT) \right]^2 \tag{3}$$

is optimized. Here $\widehat{C_t}$ is the estimate of C_t given by the model in Equation 1 with estimated values of k_a, k_{pv}, τ_a, τ_{pv}, k_1 and v_{dis} during the optimization process. T is the temporal interval between time points and N_t is the total number of time points in the DCE curves. This study used the Nelder Mead Simplex algorithm to perform the optimization.

2.2 | Linear single-input, two-compartment model

2.2.1 | Rationale

As fitting of the DITC PK model requires the optimization of six parameters, it is susceptible to overfitting of variations caused by noise, and is also time consuming when fitting a long dynamic series of data in the whole liver. Estimation of k_1 (the contrast uptake rate of hepatocytes) requires a long time period of observation of the contrast accumulation in hepatocytes. The hemodynamic changes after the initial transient time following the contrast bolus injection become slow. This offers an opportunity to solve the problem in a different manner, producing a computationally simpler problem and, ideally, reducing the susceptibility to variation. Assumptions used in the derivation and formula are described in the following subsections.

2.2.2 | Assumptions and formulation

The change in the total amount of contrast in the distribution volume in a voxel is:

$$V_{dis} \frac{dC_{dis}(t)}{dt} = V_{dis}[k_a C_a(t - \tau_a) + k_{pv} C_{pv}(t - \tau_{pv})] - V_{dis}(k_2 + k_1) C_{dis}(t) \tag{4}$$

which is Equation 2 in the derivative form. Given the long acquisition period for the observation of gadoxetic acid uptake in hepatocytes, after a few circulations of the contrast bolus in the blood ($t > t_p$), the contrast concentration in the portal vein blood is eventually equal to that in the arterial blood, $C_a(t) = C_{pv}(t)$. Under this condition, Equation 4 can be rewritten as:

$$V_{dis} \frac{dC_{dis}(t)}{dt} = V_{dis} k_t C_a(t) - (k_1 + k_2) V_{dis} C_{dis}(t) \quad \text{when } t > t_p \tag{5}$$

where $k_t = (k_a + k_{pv}) = (1 - Hct)k_2$, the normalized total blood flow rate in V_t, and Hct is hematocrit. Equation 5 can be rearranged as:

$$C_{dis}(t) = \frac{k_t}{k_1 + k_2} C_a(t) - \frac{1}{k_1 + k_2} \frac{dC_{dis}(t)}{dt} \quad \text{when } t > t_p \tag{6}$$

Substituting C_{dis} in Equation 6 into the second term in Equation 6, Equation 6 can be further rewritten as:

$$C_{dis}(t) = \frac{k_t}{k_1 + k_2} C_a(t) - \frac{k_t}{(k_1 + k_2)^2} \frac{dC_a(t)}{dt} + O\left(\frac{d^2 C_a(t)}{dt^2}\right) + \dots \quad \text{when } t > t_p \tag{7}$$

where the first term depends on C_a, the second term depends on the first derivative of C_a, the third term depends on the second derivative of C_a, and so on. If the second derivative of C_a is small enough to be neglected, substituting Equation 7 into Equation 1 and rearranging the terms, we have:

$$(1-\text{Hct})C_t(t) = v_{dis}\frac{k_2}{k_1+k_2}\left\{\left(1-\frac{k_1}{k_1+k_2}\right)C_a(t) + k_1\int_0^t C_a(\tau)d\tau - \frac{1}{k_1+k_2}\frac{dC_a(t)}{dt}\right\} \tag{8}$$

Equation 8 can be considered as the linear problem $y=ax_1 + bx_2 + cx_3$, where $y = (1 - \text{Hct})C_t(t)$ and $\vec{x} = (x_1, x_2, x_3) = \left(C_a(t), \int_0^t C_a(\tau)d\tau, \frac{dC_a(t)}{dt}\right)$.

A linear least-squares (LLS) fit can estimate the coefficients a, b and c. k_1, k_2 and v_{dis} can be solved from the coefficients (see Appendix B).

If the second term (related to the first derivative of C_a) in Equation 7 can be neglected, we have:

$$(1-\text{Hct})C_t(t) = v_{dis}\frac{k_2}{k_1+k_2}\left\{C_a(t) + k_1\int_0^t C_a(\tau)d\tau\right\} \tag{9}$$

Again, Equation 9 is a linear problem, $y = ax_1 + bx_2$, where $y = (1 - \text{Hct})C_t(t)$ and $\vec{x} = (x_1, x_2) = \left(C_a(t), \int_0^t C_a(\tau)d\tau\right)$, which can be solved by LLS fitting. In this case, $k_1 = \frac{b}{a}$. It should be noted that there is no assumption made relating to k_1 and k_2, and but k_2 and v_{dis} cannot be solved. Also, Equation 9 can be rearranged to be:

$$\overbrace{\frac{(1-\text{Hct})C_t(t)}{C_a(t)}}^{y} = \overbrace{v_{dis}k_1\frac{k_2}{k_1+k_2}}^{slope}\overbrace{\frac{\int_0^t C_a(\tau)d\tau}{C_a(t)}}^{x} + \overbrace{v_{dis}\frac{k_2}{k_1+k_2}}^{intercept} \tag{10}$$

which is a form of Patlak analysis.[12] It should be noted that k_1 can be calculated by slope/intercept, and is not affected by the relationship between k_1 and k_2, which is different from Patlak analysis. The intercept in Patlak analysis is called v_{eff} and is usually greater than the true blood distribution volume. The intercept in our case, $v_{dis}\frac{k_2}{k_1+k_2}$, is smaller than v_{dis}. However, if we assume that $k_2 \gg k_1$, v_{dis} can be estimated by the intercept. It should be noted that we only used the assumptions: $C_a(t) = C_{pv}(t)$ and that there is slow contrast change in the blood after $t > t_p$, to derive these equations. We call it the linearized single-input, two-compartment (LSITC) model hereafter.

2.2.3 | Optimization

Optimization of Equation 10 involves first computing the vector x and the set of vectors y (one for each voxel). In addition, t_p (or x_p corresponding to t_p) needs to be determined. Based on the assumptions of the model, x and y will be linearly related after x_p, suggesting that a linearity test is needed. If it is assumed that x_p is relatively consistent throughout the liver, a single test can be performed, reducing noise effects and saving computation time.

To obtain x_p, the vectors y are averaged over all voxels within the liver to form a single vector. The two singular values of the centered data matrix $[x\ y]$ after the tested x_p are acquired by the singular value decomposition. The tested x_p is varied within a time interval between the arterial peak and 2 min before the last data point. The ratio of the first singular value to the second is calculated to determine the linearity of the relationship. x_p is then chosen to maximize this ratio. Figure 2 illustrates the behavior of the y vector before and after x_p in a region of interest. However, in cases with sparse temporal sampling, the process can be simplified by setting t_p based on the DCE data with high temporal sampling.

After selection of x_p, total least-squares regression is performed for each voxel using the data after x_p to minimize the impact of errors in both x and y. The slope of the resulting fit is divided by the intercept to determine the value of k_1 in the voxel. In cases in which the intercept is less than 0.02, k_1 is set to zero to prevent values from blowing up. This is also justified in that a low intercept, corresponding to a sufficiently low v_{dis}, will effectively preclude meaningful levels of uptake in the voxel.
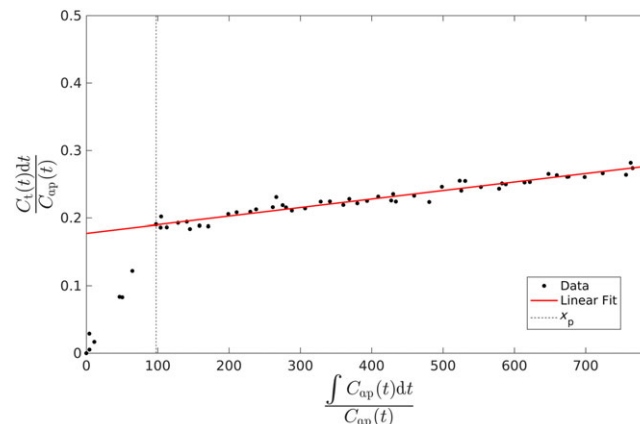

FIGURE 2 An example of the relationship between the vectors y and x in Equation 10 from a volume of interest in the liver. Note that the linear assumptions of the model only bear out after the transition point x_p

2.3 | Evaluation

This study evaluates the performance of the LSITC model, with reference to the results of six parameter optimization of the established DITC model, simulated data based on the DITC model, global liver function assessment through ICG retention in the plasma and a comparison with literature values.

2.3.1 | Data acquisition

In order to compare the results of the proposed LSITC model with the DITC model, three-dimensional (3D) volumetric DCE MRI of the liver was acquired during the intravenous injection of a single standard dose of gadoxetic acid using a golden-angle radial sampling volume-interpolated breath-hold examination on a 3-T scanner (Skyra, Siemens Healthineer, Tarrytown, New York, United States) in a prospective protocol approved by the University of Michigan Institutional Review Board. Fourteen examinations from 13 patients with intrahepatic cancers were acquired prior to radiation therapy during free breathing. The demographic, pathological and clinical Child–Pugh scores of this group of patients (called Group 1) are provided in Table 1. It should be noted that 54% of the patients had Child–Pugh scores of 5, indicating good liver function. In this group of patients, 3D DCE images were acquired with temporal resolutions of 3.5–10 s and total acquisition times of 4–24 min, and covered the whole liver with 64–72 slices with slice thicknesses of 2.6–4.5 mm and in-plane resolution of 2.1 mm × 2.1 mm to 2.4 mm × 2.4 mm (192 × 192 pixels). These scans are referred to as high-temporal-resolution (HTR) scans. The HTR scans could be fitted to both the DITC and LSITC models, allowing comparison of the results obtained from the two methods.

In addition, the proposed LSITC model was applied to clinical multiphase MRI with gadoxetic acid in 19 patients, which was approved by a retrospective protocol of the University of Michigan Cancer Center. The demographic, pathological and clinical Child–Pugh scores of this second group of patients are provided in Table 1. Pre- and post-radiotherapy scans were acquired from 19 patients, for a total of 40 scans. Each patient had been diagnosed with hepatocellular carcinoma (HCC). The scans comprised 3D volumetric multiphase MRI of the liver during the intravenous injection of a single standard dose of gadoxetic acid on either a 1.5-T GE (Chicago, Illinois, United States) or 1.5-T Philips (Andover, Massachusetts, United States) scanner. Each examination consisted of a pre-contrast volume, three-phase (arterial and portal vein phases) volumes that were each spaced approximately 20 s apart, and hepatobiliary phase volumes at approximately 10 and 20 min post-contrast, for a total of six time points. Each acquisition was obtained during a breath-hold. 3D MRI involved 88–124 slices per volume with 256 × 256 pixels to 512 × 512 pixels in the plane. The pixel size varied from 0.7 mm × 0.7 mm to 1.4 mm × 1.4 mm within each slice, with the slice thickness consistently at 2 mm. These scans are referred to as low-temporal-resolution (LTR) scans. However, as a result of changes in flip angle between phases in the scan (particularly in the late phases) and image quality issues, the set of usable scans was only 27 of the original 40. ICG retention examinations were carried out near the time of the scan for 20 of the 27 scans, without radiotherapy or any other treatment having taken place in the meantime. The ICG retention score as a quantitative overall liver function assessment was measured as the percentage of the original ICG dose remaining 15 min after injection, as described previously,[10] with higher plasma retention signifying poorer liver function. The patients in this second group had a median baseline ICG retention of 37.2%, with minimum and maximum retention scores of 9.8% and 50.2%, respectively.

TABLE 1 The demographic, pathological and clinical Child–Pugh scores for the patient groups used

Characteristic	Group 1 (HTR) (n = 13)	Group 2 (LTR) (n = 19)	Total (n = 32)
Median age (range) (years)	60.7 (56.5–72.0)	61.1 (52.7–78.9)	61.0 (52.7–78.9)
Gender			
Male	10 (77%)	14 (74%)	24 (75%)
Female	3 (23%)	5 (26%)	8 (25%)
Cirrhosis			
Positive	8 (62%)	16 (84%)	24 (75%)
Negative	5 (38%)	3 (16%)	8 (25%)
Histology			
Hepatocellular carcinoma	9 (69%)	18 (95%)	27 (84%)
Adenocarcinoma	2 (15%)	1 (5%)	3 (9%)
Intrahepatic cholangiocarcinoma	1 (8%)	0 (0%)	1 (3%)
Solitary fibrous tissue	1 (8%)	0 (0%)	1 (3%)
Baseline Child–Pugh score			
5	7 (54%)	5 (26%)	12 (38%)
6	4 (31%)	7 (37%)	11 (34%)
7	0 (0%)	5 (26%)	5 (16%)
8	1 (8%)	1 (5%)	1 (3%)
9	1 (8%)	0 (0%)	1 (3%)
Missing	0 (0%)	1 (5%)	1 (3%)

2.3.2 | Image pre-processing

For the clinical LTR multiphase images, interpolation was carried out on the image volumes that had different spatial resolutions between the volumes. All 3D multiphase LTR MRI volumes in an examination were co-registered using a robust, over-determined image registration method.[13] For all volumes, the aorta was contoured from the aortic split to the liver up to 3 cm. The 100 voxels within this region that had the highest contrast just before the arterial concentration peak were averaged to form the AIF. For the HTR DCE data, the portal vein was also contoured and selected by the same process to obtain the PVIF. In both cases, RE was used to create the input functions:

$$C(iT) \propto \frac{SI_i}{SI_{pre-contrast}} - 1 \tag{11}$$

where $C(iT)$ describes the relevant concentration at time point i, given a sampling interval of T, and SI_i and $SI_{pre-contrast}$ are the average signal intensities in the given region of interest at time point i and prior to contrast enhancement, respectively. The same calculation was performed for each voxel in the liver.

2.3.3 | Evaluation metrics

k_1 maps were obtained from the HTR DCE series using both the established DITC model and the proposed LSITC model. The k_1 maps obtained from the DITC approach were used as a reference standard in the evaluation of the LSITC approach.

The first evaluation was to assess the similarity and deviation between the two resulting k_1 maps within the liver. The similarity was tested by the linear correlation coefficient between the two k_1 maps. The deviation was evaluated by the weighted mean absolute percentage error (WMAPE), where we define the voxel-wise weighted absolute percentage error (WAPE) as:

$$\frac{|reference(i) - estimate(i)|}{\frac{1}{N}\sum_{n=1}^{n=N} reference(n)}. \tag{12}$$

where i and n are voxel indices, and N is the total number of voxels considered. It should be noted that this metric places higher weight on accuracy for larger measurements. In this case, the DITC model uptake rates are the reference values.

The second evaluation was to assess the validity of the LSITC model as applied to the clinical multiphase LTR MRI data. As a result of the low temporal resolution of approximately 20 s, the AIF peak could be missed or averaged over 20 s of sampling. The sampling of the arterial peak affects the integral of the AIF in Equation 10. Considering that the integral is over a long time period of 10–20 min, the effect of the arterial peak on the k_1 estimation could be small. To evaluate it, a tissue concentration curve with a temporal resolution of 1/s was simulated by direct application of the DITC model, subject to the input of reasonable parameter values and blood concentration curves. To mimic the LTR multiphase MRI data, a subsampled curve was created by removing all points after the first pre-contrast point and prior to the peak of the AIF. This curve was used to assess the error inherent in neglecting to sample the upswing in the arterial function, even when the image was perfectly timed to correspond to the peak. In order to evaluate the additional bias incurred by mistiming the peak, an additional concentration curve was created by removing all post-contrast data until 20 s after the arterial peak. This mimics a 20-s delay in the ideal time to image the arterial peak. For each of these three cases, the primary metrics were the correlation coefficients and WMAPE. The error in the k_1 estimation could represent an upper bound on the error incurred by missing the arterial peak, as acquisition delays longer than this would be easily visually recognizable.

The third assessment involved the application of the LSITC approach to the clinical multiphase MRI data and comparison with global liver function as measured by the ICG retention rates. These clinical scans were much sparser temporally than those seen in the HTR DCE scans, and so fitting with the full DITC model was impractical. The metric for evaluation was the correlation coefficient between the sum of the estimated K_1 values over the contoured liver volume by the LSITC approach and the logarithm of the ICG retention score, where $K_1 = k_1 V_{dis}$. In the sum of K_1 over the whole contoured liver volume, outliers having K_1 values above the 95th or below the 5th percentiles were rejected to remove edge effects. In addition, large vessels were excluded by rejecting voxels in which v_{dis} was greater than 0.4. The inclusion of the volume term ensures that both the uptake rate and plasma flow are accounted for. The summation of a regional measure of liver function to allow comparison with a global function, such as ICG, is not new.[14]

The final assessment involved comparison of the k_1 values obtained in the HTR DCE and LTR multiphase MRI datasets with reported values of k_1 in the liver from previous studies.

3 | RESULTS

3.1 | k_1 estimations by the LSITC model *versus* DITC model

Maps of k_1 values estimated from the liver HTR DCE scans using both the LSITC and DITC models are shown in Figure 3.

The linear correlations between the k_1 maps estimated by the two models are shown in Figure 4. The correlation was calculated in a randomly selected 5000 voxels within each liver, restricted to the voxels in which v_{dis} was above the 25th and below the 75th percentiles, and the k_1 values
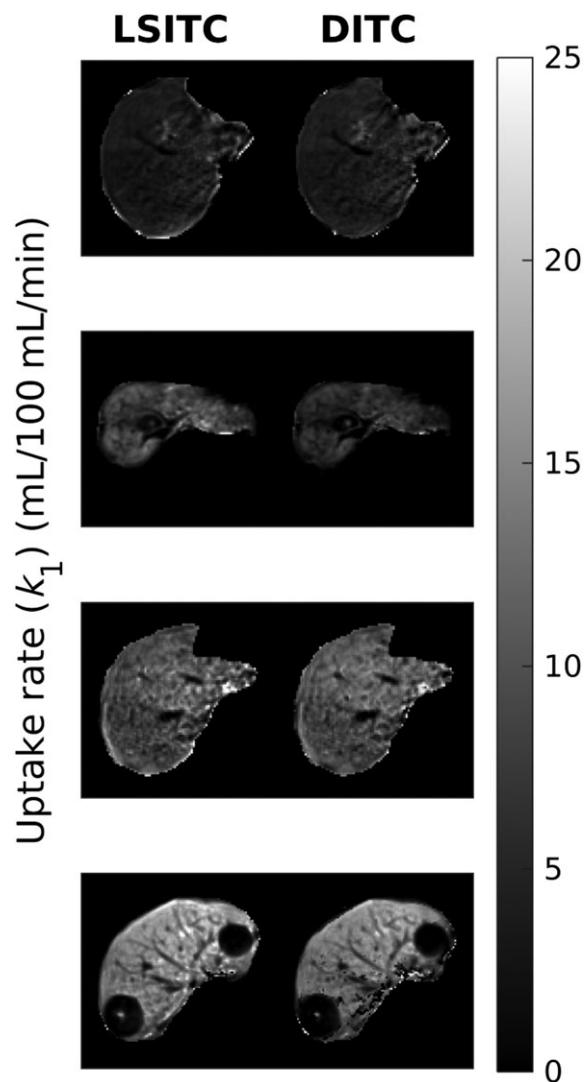
FIGURE 3 Example slices of the k_1 maps estimated from the high-temporal-resolution, dynamic contrast-enhanced (HTR DCE) scans of four patients by the linearized single-input, two-compartment (LSITC) model (left) and dual-input, two-compartment (DITC) model (right). Note that the units are mL/100 mL/min

were greater than 0.01 mL/100 mL/min. (In one patient who was a candidate for a liver transplant and had a very poor liver function, there was a small volume in the liver that had non-zero k_1 values, leaving little volume for analysis. Thus, this patient was excluded from the analysis described here.) The correlation coefficients ranged from 0.98 to 0.76, with a median of 0.91. The WMAPEs ranged from 9.0% to 39.4%, with a median of 17.2%. It should be noted that either estimate can be considered as the ground truth.

The estimated transition times (t_p) varied from 10 to 313 s as measured from the peak of the AIF, with a median value of 58 s. The computational speed of the LSITC approach was approximately 1000 times faster than that of the DITC model, taking a few seconds per examination, whereas DITC model fitting took several hours per examination.

3.2 | k_1 estimation by simulation of missing of the arterial peak

To simulate DCE data, composite input curves were first created by averaging the respective AIF and PVIF after matching the arterial peaks and resampling the time curves from all patients. The composite functions converged approximately 75 s after the arterial peak. To reduce noise, the input data at least 5 min subsequent to the arterial peak were replaced by a double exponential fit.

The simulated parameters were randomly chosen but uniformly distributed over the ranges shown in Table 2, whereas τ_a and τ_{pv} were assumed to be 0 s. Using these values and the composite input concentration curves (AIF and PVIF), the resulting tissue concentration curves were calculated using the DITC model.

To assess the potential error and variance incurred by missing the arterial peak during the clinical multiphase MRI scan, the resulting tissue and arterial functions (Figure 5a) were subsampled to remove all points prior to the arterial peak, apart from one pre-contrast reference scan
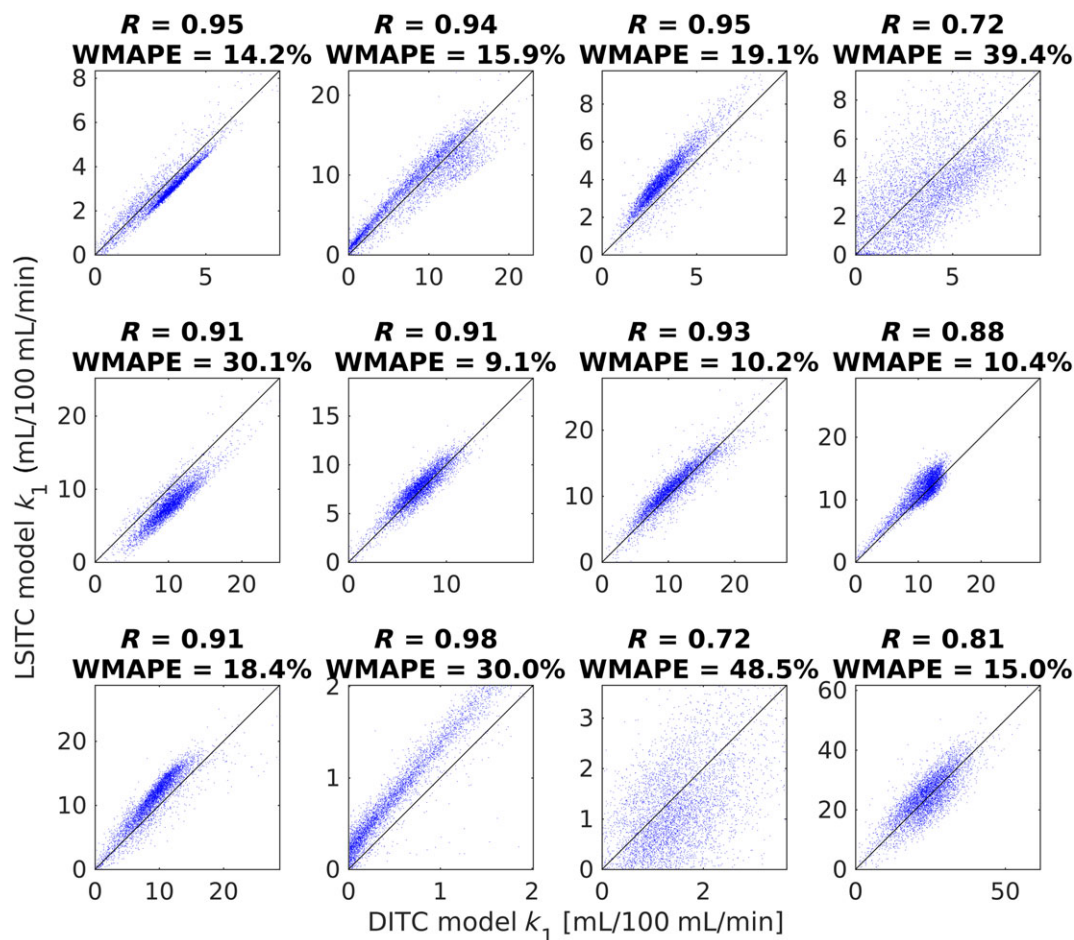
FIGURE 4 Scatter plot of the k_1 values estimated by the two models for the eight patients. The k_1 values on the horizontal axis were estimated from the dual-input, two-compartment (DITC) model and those on the vertical axis were estimated from the linearized single-input, two-compartment (LSITC) model

TABLE 2 The ranges of parameter values for the simulation, where $k_{pvp} = k_{pv}(1 - Hct)$ and $k_{ap} = k_a(1 - Hct)$ (Hct, hematocrit)

Parameter	Minimum value	Maximum value	Unit
v_{dis}	10	20	%
$k_{pvp} + k_{ap}$	50	300	mL/100 mL/min
k_{pvp}	$0.5(k_{pvp} + k_{ap})$	$(k_{pvp} + k_{ap})$	mL/100 mL/min
k_1	0	$0.1(k_{pvp} + k_{ap})$	mL/100 mL/min

(Figure 5b). Furthermore, the data points acquired 20 s after the arterial peak (including the peak) were removed from the simulated curve and AIF to mimic a possible further delayed acquisition in the clinical data (Figure 5c).

For each scenario, t_p was assumed to be 60 s post-peak. The simulation was run 10 000 times per case. A strong correlation was found between the LSITC results and input simulation values. Without noise, correlation coefficients remained above 0.99 for all three cases, including the case with an acquisition delay of 20 s after the arterial peak.

The results showed similar distributions for estimates of k_1, regardless of the acquisition delay (see Figures 6 and 7). The WAPE in the noise-free simulations was 4.7 ± 3.2% (mean ± standard deviation) for the full dataset, shifted to 6.1 ± 3.6% for the data missing time points before the arterial peak and to 6.7 ± 2.4% for the data missing time points up to 20 s after the arterial peak. The WAPE changed little when introducing white Gaussian noise to the generated C_t functions. It should be noted that missing the early time points in the dynamic curves caused a maximum change in the WAPE of 2% (from 4.7 to 6.7% without noise), suggesting that other effects predominate in the k_1 estimation errors. Based on these results, we would expect similar levels of systematic error resulting from delayed or averaged capture of the arterial peak in the LTR multiphase data.
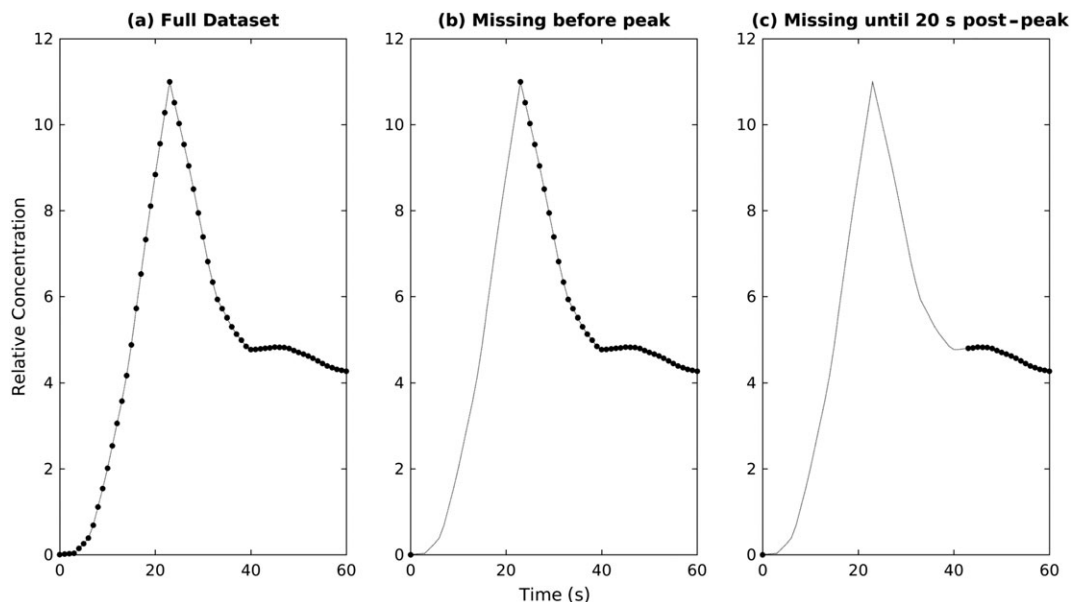
FIGURE 5 Early section of the arterial input functions (AIFs) to demonstrate subsampling used to investigate delays in acquisition. (a) AIF with the full dataset. (b) AIF with missing data points prior to the arterial peak. (c) AIF with missing data points up to 20 s after the arterial peak
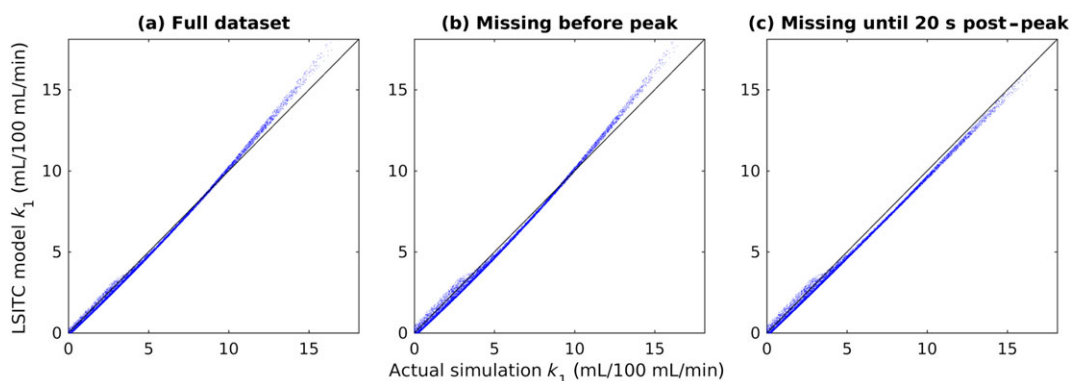

FIGURE 6 Plots of the input k_1 values against the k_1 values obtained by the linearized single-input, two-compartment (LSITC) model. The correlation coefficients R were 0.999, 0.998 and 0.999 for the full dataset (a), the dataset missing time points prior to the arterial peak (b) and the dataset missing time points up to 20 s after the arterial peak (c), respectively

3.3 | k_1 estimation from clinical MRI and comparison with ICG retention

Maps of k_1 and v_{dis} were estimated from the clinical LTR multiphase MRI of 27 examinations using the LSITC model. Example k_1 and v_{dis} maps are shown in Figure 8. For the 20 clinical scans with accompanying ICG retention scores, the scores were compared with the K_1 values ($K_1 = k_1 V_{dis}$) summed over the contoured liver volume (Figure 9). Voxels with v_{dis} greater than 0.4 were rejected to omit vasculature, and K_1 values less than the 5th or greater than the 95th percentiles were rejected to avoid outliers and edge effects. As the logarithm of ICG retention is inversely proportional to the rate of clearance in the liver, a linear relationship is expected. The sum of K_1 values was significantly correlated with the logarithm of ICG retention values with a correlation coefficient of $R = -0.72$ ($p = 0.0004$, $n = 20$).

3.4 | Comparison with literature values

Maps of k_1 values were generated for the 27 multiphase LTR liver scans by the LSITC model. In each of the 27 k_1 maps, the mean value was calculated over the volume with v_{dis} less than 0.4 and with k_1 values in the central 90th percentile of the k_1 value for the liver. The mean value across all multiphase LTR scans was 3.93 ± 1.79 mL/100 mL/min. Using the same process for the HTR DCE-based maps, the mean uptake was measured as 9.17 ± 8.23 mL/100 mL/min across all HTR DCE scans, and 7.44 ± 4.93 mL/100 mL/min after removal of an outlier more than twice as large as any other mean uptake. It should be noted that the outlier was also the scan with the shortest total duration.

This is fairly consistent with previous literature. Previous studies have found mean uptake rates of 3.4 ± 2.1 mL/100 mL/min in background regions of livers with metastases, 3.03 ± 2.1 mL/100 mL/min in cirrhotic livers and 6.53 ± 2.4 mL/100 mL/min in healthy livers, as shown in Figure 10.[15,16]
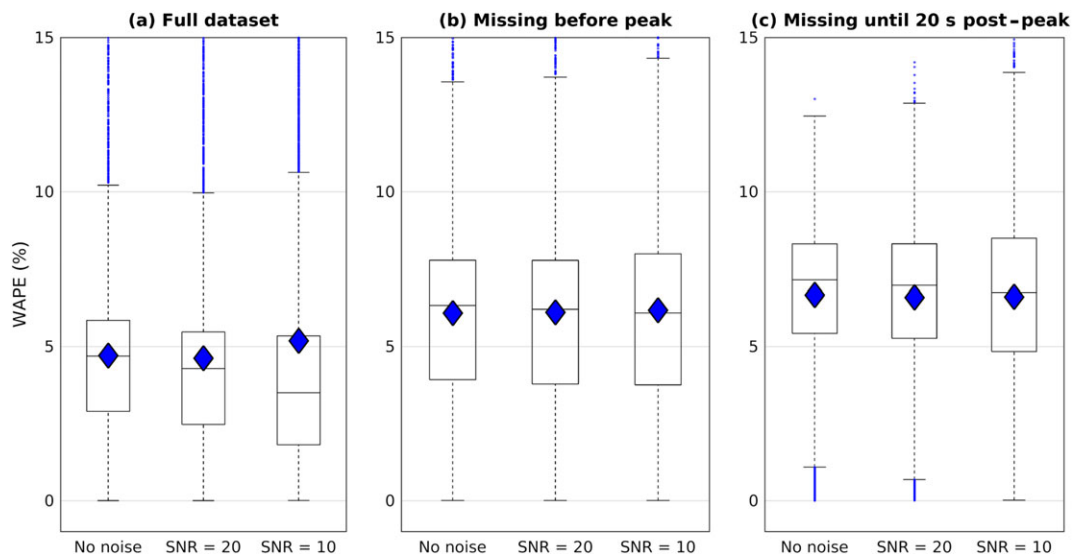
FIGURE 7 Boxplots for the weighted absolute percentage error (WAPE) in the linearized single-input, two-compartment (LSITC) model results, relative to the simulated values, at three noise levels for the three simulated datasets: (a) the full dataset; (b) the dataset missing data points prior to the arterial peak; (c) the dataset missing data points up to 20 s after the arterial peak. The median values are indicated by the horizontal line, the mean is indicated by the diamond and error bars are 1.5 times the interquartile range
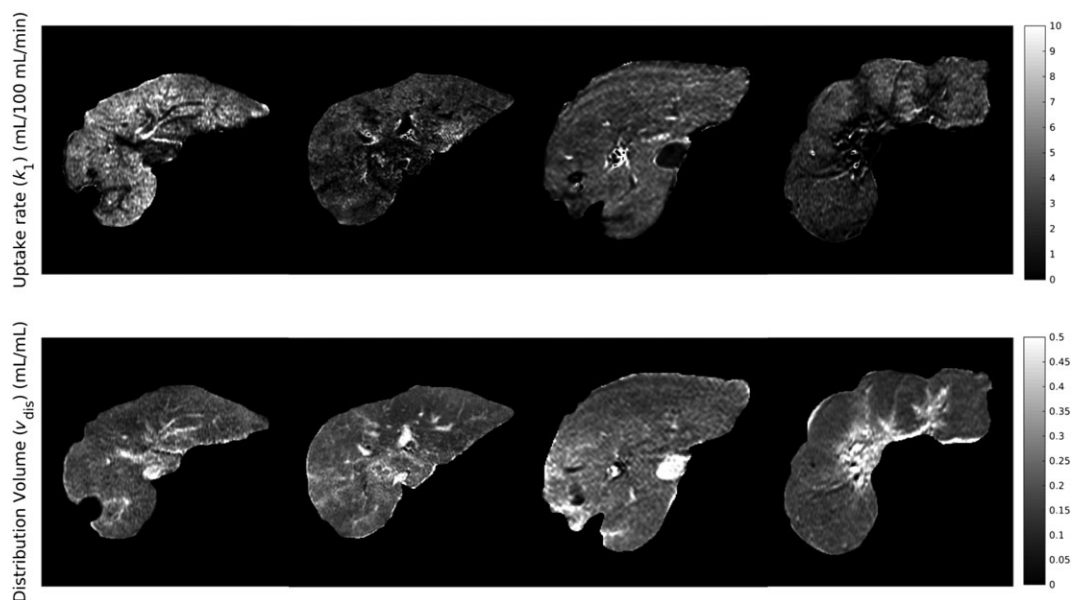
FIGURE 8 Example maps of k_1 and v_{dis} in the assessed livers. High values of v_{dis} can be seen to correspond to the vasculature

4 | DISCUSSION

In this study, we developed an LSITC model to quantify k_1 from dynamic gadoxetic acid-enhanced MRI in the liver, and evaluated the results by comparison with an established uptake model and the measurement of whole liver function. The k_1 values estimated by LSITC and DITC analysis of the HTR DCE MRI data showed a close median correlation ($R = 0.91$). Application of the LSITC approach to LTR multiphase MRI data gave similar results to previous studies and correlated relatively well ($R = -0.72$) with the results of ICG retention examinations. Furthermore, concerns about the impact of delayed imaging of the arterial peak were addressed by simulations showing less than 3% related error. The results indicate that the LSITC model is a simple analog to the DITC model, and correlates well with independent scores of liver function. As this technique can be applied to clinically typical multiphase data, it presents the possibility of quantitative liver assessment without large changes to existing clinical workflow.

There are several possible sources of error in the determination of k_1 via the LSITC model proposed here. First, it should be noted that, unlike the Patlak model, the ratio of k_1 to k_2 should not impact the estimate of k_1, as the k_2-dependent term cancels in Equation 10 when dividing the
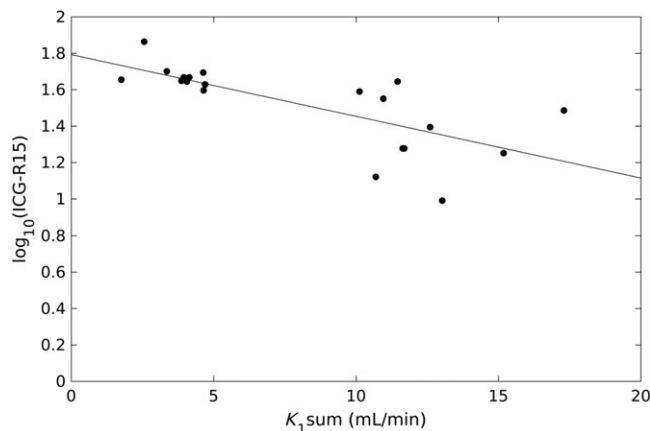
FIGURE 9 Plot of the logarithm of indocyanine green (ICG) retention at 15 min against the sum of K_1 values in the contoured total liver volume. $R = -0.72$ ($p = 0.0004$, $n = 20$)
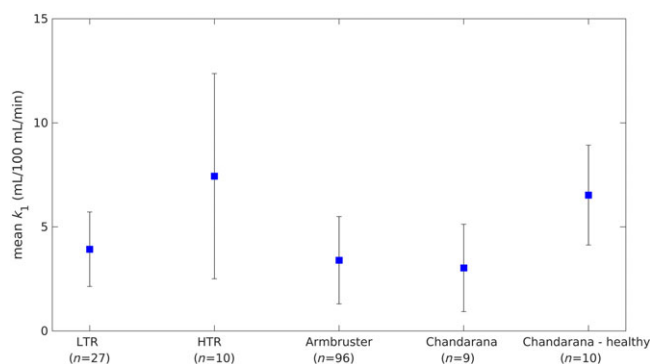

FIGURE 10 This plot shows the mean values obtained in several studies for the background liver uptake rate of gadoxetic acid in cancerous livers and in a group of healthy livers for reference. Error bars indicate the standard deviation. The HTR values are based on a removed outlier. HTR, high-temporal-resolution; LTR, low-temporal-resolution. The mean uptake rate for Armbruster was 3.4 ± 2.1 (n=96). For Chandarana the mean uptake rate was 3.03 ± 2.1 (n=9) in cirrhotic livers, and 6.53 ± 2.4 (n=10) in healthy livers

slope by the intercept. However, this term will impact the estimate of v_{dis} and K_1, with both underestimated. This also suggests a more complete linear model when Equation 8 is fitted to determine k_1, k_2 and v_{dis}, allowing a more accurate estimate of K_1 (see Appendix B).

The model assumes that, after t_p, $C_{pv} = C_a$. In most of the measured input curves, C_a and C_{pv} were very similar within less than 1 min of the arterial peak. In some cases, this held true after a constant correction factor, i.e. $C_{pv} \times$ constant $= C_a$. This could reflect differences in Hct between C_a and C_{pv}. In the quantification of C_a and C_{pv}, native T_1 of plasma was not considered, as images for T_1 quantification are almost never acquired in clinical liver scans. However, native T_1 of plasma should be the same for C_a and C_{pv}. This omission should not contribute to the difference between C_a and C_{pv}. In general, it is anticipated that the peak of C_{pv} will be shallower and broader than that of C_a, as the bolus of contrast travels through the vascular systems of intestines and spleen before it slowly returns to the portal vein through the mesenteric vein and splenic vein. In some patients, this contrast return seems to be slower than in others. This could be a factor contributing to the difference between C_a and C_{pv} even after the typical time t_p. However, partial volume effects and motion could also affect the measurement of C_{pv}, causing apparent differences between C_{pv} and C_a that do not reflect the actual contrast concentrations. The simplified form of the model also neglects dC_a/dt from Equation 8. As dC_a/dt will generally be negative, and decreasing in magnitude after t_p, we expect this to result in a small overestimate of v_{dis} and k_1. The possibility of flow-related enhancement causing a mischaracterization of AIF can also be considered. Selection of the AIF values from an aorta contour within 3 cm of the aortic split to the liver ensured that the blood in the voxels used was far from the edge of the field of view, and had experienced multiple repetitions within the excitation volume. This minimizes the impact of flow-related enhancement on the AIF, making this an unlikely source of error in AIF, or cause of differences between AIF and PVIF. The estimate of x_p could also impact the final solution. Choosing x_p too early would be expected to cause an underestimate of v_{dis}, and an overestimate of k_1. In the absence of noise, even a very late estimate of x_p should have little impact on the result. However, with noise, we would expect additional uncertainty in the result, as we estimate the slope and intercept from fewer data points.

In the LTR clinical data, we assumed that the last three points after enhancement were after t_p. This was necessary to obtain an overdetermined solution, but may not have been accurate in some voxels or livers. The time post-arterial peak for the first point in the fit varied between 36 and 290 s. The median time was 48 s. This can be compared with the optimal t_p times chosen in the HTR data, which had a median of 65 s. It should be noted that the peak in the LTR clinical data was assumed to coincide with the start of the first post-contrast image, and so it is possible that there is a hidden delay

relative to the physiological arterial peak. Another possible source of error is the sparsity of the clinical data, which causes an underestimate of the integral of C_a, and thus an underestimate of the values for x. We would expect this error to increase as the timing of the first post-contrast measurement was delayed past the peak, but the change in error in the simulation was relatively minor, indicating that other effects predominate.

Both the LSITC and DITC models omit several notable features. First, the models omit the excretion of contrast from the hepatocytes into the bile. It was assumed that the rate of excretion was negligible over the timeframe of the examinations. Deviations from this assumption would cause error in k_1 and thus impact the total functional estimate. However, this would not impact the comparison between the two models, or affect the error in the simulated case. Second, the DITC model includes only one extracellular compartment, which may not be valid in tumors or other pathological tissues where movement between the capillary bed and the space of Disse is relatively slow. This would again impact both models. The impact could be assessed by comparison with a dual-input, three-compartment model.[17]

The contrast concentration for all examinations was calculated using RE. RE has been found to correlate linearly with the concentration in a given tissue, although this relationship breaks down at sufficiently high contrast concentrations.[17] However, even if we assume perfect linearity and that all plasma and all liver voxels had uniform respective native T_1 values, the direct use of RE as the relative concentration will introduce a constant bias term in the uptake rate based on the native T_1 in plasma relative to liver tissue. This would not impact the correlation with liver function and could be fixed through a correction constant with knowledge of the ratio of native liver and plasma T_1. If we further consider differences in native T_1 across the liver, we would expect additional error even in the relative voxel-wise uptake rate. This could be fixed by characterizing the pre-contrast T_1 with an additional sequence before contrast injection. Ideally, this would allow for more accurate quantification of concentration, but introduces clinical inconvenience and complicates the analysis.

In all real data, noise, motion and other random variation contributed to error in the input curves and the tissue curves. Random variation will be especially harmful in cases in which relatively few data points are used in the estimate of k_1. Motion effects are especially apparent at the edges of the liver and liver vasculature. In these locations, slight motion can cause apparent jumps in uptake as a motion artifact.

Further work can be performed to improve k_1 quantification. For example, the impact of noise and motion could be lessened by the introduction of spatial regularization to the creation of the k_1 map. The full model from Equation 8 can be used if k_2 or v_{dis} are parameters of interest, although it should be noted that the LSITC model cannot replace the DITC model when arterial or portal venous perfusion are parameters of interest. An evaluation of the impact of omission of native T_1 on k_1 estimation across the population of patients should be conducted. Additional work should also use larger and more varied datasets to further characterize the relationship between liver function and uptake as measured by the LSITC model. Further analysis should also consider tissues in which the DITC model is insufficient and include comparison with a dual-input, three-compartment model.[17]

5 | CONCLUSION

This work proposes and validates the LSITC model for the assessment of liver function based on the uptake rate of gadoxetic acid. Validation was obtained relative to the predictions[17] of the accepted DITC model and independent measurements of whole liver function. The LSITC approach allows the creation of a spatially resolved quantitative image of liver function, using standard clinical acquisitions, and removes the requirement for impractical, high-temporal-resolution scans.

ORCID

Josiah Simeth 🔟 http://orcid.org/0000-0001-6847-565X

REFERENCES

1. Johnson PJ, Berhane S, Kagebayashi C, et al. Assessment of liver function in patients with hepatocellular carcinoma: a new evidence-based approach— the ALBI grade. *J Clin Oncol*. 2015;33(6):550-558.

2. Wu VW, Epelman MA, Wang H, et al. Optimizing global liver function in radiation therapy treatment planning. *Phys Med Biol*. 2016;61(17):6465-6484.

3. Bennink RJ, Cieslak KP, van Delden OM, et al. Monitoring of total and regional liver function after SIRT. *Front Oncol*. 2014;4.

4. Wang H, Feng M, Frey KA, Ten Haken RK, Lawrence TS, Cao Y. Predictive models for regional hepatic function based upon ^{99m}Tc-IDA SPECT and local radiation dose for physiological adaptive RT. *Int J Radiat Oncol Biol Phys*. 2013;86(5):1000-1006.

5. Sørensen M, Mikkelsen KS, Frisch K, Villadsen GE, Keiding S. Regional metabolic liver function measured by 2-[^{18}F]fluoro-2-deoxy-D-galactose PET/CT in patients with cirrhosis. *J Hepatol*. 2013;58(6):1119-1124.

6. Cao Y, Wang H, Johnson TD, et al. Prediction of liver function by using magnetic resonance-based portal venous perfusion imaging. *Int J Radiat Oncol Biol Phys*. 2013;85(1):258-263.

7. Bormann RL, da Rocha EL, Kierzenbaum ML, Pedrassa BC, Torres LR, D'Ippolito G. The role of gadoxetic acid as a paramagnetic contrast medium in the characterization and detection of focal liver lesions: a review. *Radiol Bras*. 2015;48(1):43-51.

8. Yamada A. Quantitative evaluation of liver function within MR imaging. In: El-Baz AS, Saba L, Suri J, eds. *Abdomen and Thoracic Imaging*. Town: Springer US; 2014:233-251.

9. Sourbron S, Sommer WH, Reiser MF, Zech CJ. Combined quantification of liver perfusion and function with dynamic gadoxetic acid-enhanced MR imaging. *Radiology*. 2012;263(3):874-883.

10. Stenmark MH, Cao Y, Wang H, et al. Indocyanine green for individualized assessment of functional liver reserve in patients undergoing liver radiation therapy. *Int J Radiat Oncol Biol Phys*. 2013;87(2):S26-S27.

11. Van Beers BE, Pastor CM, Hussain HK. Primovist, Eovist: what to expect? *J Hepatol*. 2012;57(2):421-429.

12. Patlak CS, Blasberg RG. Graphical evaluation of blood-to-brain transfer constants from multiple-time uptake data. Generalizations. *J Cereb Blood Flow Metab*. 1985;5(4):584-590.

13. Johansson A, Balter J, Feng M, Cao Y. An overdetermined system of transform equations in support of robust DCE-MRI registration with outlier rejection. *Tomography: J Imaging Res*. 2016;2(3):188-196.

14. Yoneyama T, Fukukura Y, Kamimura K, et al. Efficacy of liver parenchymal enhancement and liver volume to standard liver volume ratio on Gd-EOB-DTPA-enhanced MRI for estimation of liver function. *Eur Radiol*. 2014;24(4):857-865.

15. Chandarana H, Block TK, Ream J, et al. Estimating liver perfusion from free-breathing continuously acquired dynamic gadolinium-ethoxybenzyl-diethylenetriamine pentaacetic acid-enhanced acquisition with compressed sensing reconstruction. *Invest Radiol*. 2015;50(2):88-94.

16. Armbruster M, Zech CJ, Sourbron S, et al. Diagnostic accuracy of dynamic gadoxetic-acid-enhanced MRI and PET/CT compared in patients with liver metastases from neuroendocrine neoplasms. *J Magn Reson Imaging*. 2014;40(2):457-466.

17. Sommer WH, Sourbron S, Huppertz A, Ingrisch M, Reiser MF, Zech CJ. Contrast agents as a biological marker in magnetic resonance imaging of the liver: conventional and new approaches. *Abdom Imaging*. 2012;37(2):164-179.

APPENDIX A

FORMULATION OF DUAL-INPUT, TWO-COMPARTMENT EQUATIONS

The change in the total amount of contrast in the distribution volume in a voxel is:

$$V_{dis}\frac{dC_{dis}(t)}{dt} = F_{ap}C_{ap}(t-\tau_a) + F_{pvp}C_{pvp}(t-\tau_{pv}) - (F_{ap} + F_{pvp} + K_1)C_{dis}(t) \tag{A1}$$

where F_{ap} and F_{pvp} are the total amounts of arterial blood plasma flow and portal vein blood plasma flow in the distribution space in the voxel, respectively, and K_1 is the amount of contrast taken up by cells per second in the voxel. F_{ap}, F_{pvp} and K_1 have units of vol/s.

The change in the total amount of agent in the intracellular volume in the voxel is:

$$V_i\frac{dC_i(t)}{dt} = K_1 C_{dis}(t) \tag{A2}$$

where V_i is the intracellular volume in the voxel.

Equation A1 can be rewritten as

$$V_{dis}\frac{dCdis(t)}{dt} = F_{ap}C_{ap}(t-\tau_a) + F_{pvp}C_{pvp}(t-\tau_{pv}) - \left[\frac{F_{ap} + F_{pvp} + K_1}{V_{dis}}\right]V_{dis}C_{dis}(t.) \\ = F_a C_a(t-\tau_a) + F_{pv}C_{pv}(t-\tau_{pv}) - (k_2 + k_1)V_{dis}C_{dis}(t) \tag{A3}$$

where $k_2 = (F_{ap} + F_{pvp})/V_{dis}$ and $k_1 = (K_1)/V_{dis}$, both of which are rates in units of inverse seconds. F_a and F_{pv} are the total amounts of arterial blood and portal vein blood flow, respectively. Here, we use the relationship $F_tC_t = F_pC_p + F_{red}C_{red}$, which means that the total amount of blood flow times the total concentration of agent in the blood is equal to the amount of blood plasma flow times the concentration of agent in plasma plus the amount of blood red cell flow times the concentration of agent in red cells. As C_{red} is zero, $F_tC_t = F_pC_p$ (agent does not enter red cells). Also, we cannot measure the concentration of agent in plasma, but can measure the concentration of agent in total blood.

Using hematocrit (Hct), we have $k_2 = [(1 - Hct)(F_a + F_{pv})]/V_{dis}$.

The solution of Equation A3 is:

$$V_{dis}C_{dis}(t) = \int_0^t [F_a C_a(\tau-\tau_a) + F_{pv}C_{pv}(\tau-\tau_{pv})] e^{-(t-\tau)(k_2+k_1)}d\tau \tag{A4}$$

The solution of Equation A2 is:

$$V_i C_i(t) = K_1 \int_0^t C_{dis}(\tau) d\tau \tag{A5}$$

The total account of contrast in the voxel is:

$$V_t C_t(t) = V_{dis} C_{dis} + V_i C_i + V'_e C'_e = V_{dis} C_{dis} + V_i C_i \tag{A6}$$

where C'_e is zero.

The final solution of the total amount of agent in a voxel or volume of interest is:

$$V_t C_t(t) = \int_0^t [F_a C_a(\tau - \tau_a) + F_{pv} C_{pv}(\tau - \tau_{pv})] e^{-(t-\tau)k_2} d\tau + K_1 \int_0^t C_{dis}(\tau) d\tau \tag{A7}$$

The unknown parameters in Equation A7 are F_a, F_{pv}, k_2 (or V_{dis}), K_1, τ_a and τ_p.

Conventionally, we present blood flow in density, so that, after quantification of F_a, F_{pv} and K_1 per voxel or per volume of interest, we need to calculate $F_a(F_{pv}$ or $K_1)/V_{dis}$.

We can rewrite the solutions of Equations A4 and A5 as:

$$V_{dis} C_{dis}(t) = \int_0^t [F_a C_a(\tau - \tau_a) + F_{pv} C_{pv}(\tau - \tau_{pv})] e^{-(t-\tau)k_2} e^{-(t-\tau)k_1} d\tau$$
$$= V_{dis} \int_0^t [F_a C_a(\tau - \tau_a) + F_{pv} C_{pv}(\tau - \tau_{pv})] e^{-(t-\tau)k_2} e^{-(t-\tau)k_1} d\tau \tag{A8}$$

$$V_i C_i(t) = K_1 \int_0^t C_{dis}(\tau) d\tau = k_1 \int_0^t V_{dis} C_{dis}(\tau) d\tau \tag{A9}$$

Therefore, we can combine Equations A8 and A9 to rewrite Equation A6 as Equations A10 and A11:

$$\overbrace{V_t C_t(t)}^{\text{Agent in Tissue}} = \overbrace{V_{dis} C_{dis}(t)}^{\text{Extracellular Agent}} + \overbrace{k_1 \int_0^t v_{dis} C_{dis}(\tau) d\tau}^{\text{Intracellular Agent}} \tag{A10}$$

$$V_{dis} C_{dis}(t) = V_{dis} \int_0^t (k_a C_a(\tau - \tau_a) + k_{pv} C_{pv}(\tau - \tau_{pv})) e^{-(t-\tau)(k_2 + k_1)} d\tau \tag{A11}$$

APPENDIX B

SOLUTION TO THREE-PARAMETER LINEARIZATION

We can recast Equation 8 in the form $y = ax_1 + bx_2 + cx_3$, where:

$$y = (1 - Hct) C_t(t)$$

$$\vec{x} = (x_1, x_2, x_3) = \left(C_a(t), \int_0^t C_a(\tau) d\tau, \frac{dC_a(t)}{dt} \right)$$

$$a = v_{dis} \frac{k_2}{k_1 + k_2} \left(1 - \frac{k_1}{k_1 + k_2} \right)$$

$$b = v_{dis} \frac{k_1 k_2}{k_1 + k_2}$$

$$c = -v_{dis} \frac{k_2}{(k_1 + k_2)^2}$$

Through algebraic manipulation of the final three terms, we can then solve for k_1, k_2 and v_{dis} in terms of the coefficients of this model:

$$k_2 = -\frac{a}{c} \tag{B1}$$

$$k_1 = -\frac{k_2}{2} + \sqrt{\frac{k_2^2}{4} - \frac{b}{c}} \tag{B2}$$

$$v_{dis} = \frac{b(k_1 + k_2)}{k_1 k_2} \tag{B3}$$